ISSN 2278-2540 | DOI: 10.51583/IJLTEMAS | Volume XV, Issue V, May 2026

Hydrodynamic Performance Enhancement of Offshore Production Separators: A CFD-Based Evaluation of Internal Geometry for Optimized Phase Separation

Nitonye Samson[1], Alabo Abiye Ekine[2], Nwoka Blessed Godstime[3]

[1,2,3]Department of Marine and Offshore Engineering, Rivers State University

DOI: https://doi.org/10.51583/IJLTEMAS.2026.150500156

Received: 14 May 2026; Accepted: 19 May 2026; Published: 10 June 2026

ABSTRACT

Offshore production separators often experience performance degradation due to suboptimal internal geometry, which promotes flow short-circuiting, high turbulence, and reduced phase separation efficiency. This study uses ANSYS Fluent to compare two full-scale horizontal gas-liquid separator configurations under identical steady-state conditions at 160 psia and 52 psia. Model A (simple perforated baffles) and Model B (inlet diverter, coalescer, demister, and outlet baffles) were evaluated via velocity fields, turbulent kinetic energy (TKE), and pressure profiles. At 52 psia, Model A showed maximum velocity of 16.06 m/s and maximum TKE of 5.40 m^2/s^2, while Model B recorded higher localized values (21.15 m/s, 12.30 m^2/s^2) confined to the demister region—where elevated velocity aids droplet capture rather than impairing separation. At 160 psia, Model B's maximum TKE (1.24 m^2/s^2) exceeded Model A's (0.70 m^2/s^2) by 77%, but with uniform cross-sectional flow compared to Model A's concentrated centerline jets. Gas outlet pressure drop across Model B increased from 0.1 psi at high pressure to 0.95 psi at low pressure (versus Model A's 0.2–0.3 psi), representing an acceptable trade-off for improved separation potential. The pressure difference between liquid and gas outlets reached 1.2 psi in Model B at low pressure versus 0.3 psi in Model A. These findings suggest that advanced internals may reduce stagnant zones by approximately 40–50% and localize turbulence, which could improve separation efficiency without disproportionately increasing overall pressure drop. However, direct separation efficiency metrics (e.g., droplet carryover, entrainment fraction) were not simulated and should be addressed in future work. Contribution to Clean Energy: This work supports cleaner offshore production by identifying internal geometries that potentially reduce energy intensity and greenhouse gas emissions. By minimizing turbulence-induced droplet carryover and flow short-circuiting, the proposed design may reduce fuel consumption per barrel of produced fluid and lower flaring from liquid carryover. These efficiency gains demonstrate how retrofitting existing fossil infrastructure could serve as a pragmatic pathway within Africa's just energy transition. The CFD methodology is also transferable to clean energy applications including biogas upgrading, hydrogen purification, and carbon capture systems

Keywords: Internal geometry, Turbulent kinetic energy (TKE), Velocity distribution, Demister, Pressure drop.

INTRODUCTION

Offshore oil and gas production remains significant in Africa's energy mix, but the separation of crude oil, produced water, and natural gas is often energy-intensive and inefficient. Production separators frequently suffer from poor internal geometry that creates high turbulence, flow short-circuiting, and reduced phase separation efficiency (Shoghl et al., 2021). These hydrodynamic inefficiencies can lead to increased energy waste, higher gas flaring, and greater environmental harm from liquid carryover.

In the context of Africa's just energy transition, improving the efficiency of existing energy infrastructure complements renewable energy development. Every percentage point of separation efficiency gained reduces the energy intensity of production, potentially lowering greenhouse gas emissions and decreasing the environmental footprint of ongoing operations (Nwoka et al., 2026).

ISSN 2278-2540 | DOI: 10.51583/IJLTEMAS | Volume XV, Issue V, May 2026

Computational Fluid Dynamics (CFD) has emerged as a valuable tool for diagnosing these inefficiencies without costly physical modifications. Previous studies have demonstrated the effectiveness of CFD in evaluating separator internals. Yu et al. (2024) showed that combined internal structures enhance separation efficiency by controlling vortices and velocity distribution. Ma et al. (2021) optimized internal components such as demisters and deflectors to achieve reported efficiencies above 98%. Nie et al. (2022) demonstrated how geometric optimization can improve performance without increasing pressure drop. Flaszyński et al. (2020) showed that simplified porous media modeling can capture key flow trends, making CFD practical for industrial applications.

However, a critical gap remains: few studies directly compare complete separator configurations under identical operating conditions using consistent metrics. This study addresses that gap by comparing two full-scale separator configurations: a simple baffle design (Model A) and an advanced integrated design (Model B) with inlet diverter, coalescer, demister, and outlet baffles. The evaluation focuses on velocity fields, turbulent kinetic energy distribution, and pressure profiles at two operating pressures (160 psia and 52 psia). The study does not simulate direct separation efficiency (e.g., droplet carryover fraction) but instead uses flow field surrogates as indicators of separation potential.

MATERIALS

This study used computer hardware and software for model creation and simulation. ANSYS Workbench served as the platform for geometry creation, meshing, setup, and analysis. Space Claim was used for geometry preparation, and Fluent performed the flow simulations

Separator Geometry Models

Two three-dimensional models of horizontal gas-liquid separators were developed based on typical industrial designs. Model A represents a simplified configuration containing two perforated baffles with minimal internal flow redistribution features. The vessel shell measures approximately 3 m in diameter and 10 m in length. The perforated baffles extend across the vessel cross-section with holes sized to allow flow passage while disrupting the inlet jet.

Model B incorporates a full set of internal components representing an optimized industrial design: an inlet diverter plate, calming section, coalescer assembly, demister pad near the gas outlet, and outlet baffles near the liquid outlets.

Both models share the same overall vessel dimensions. The only differences are the presence and type of internal components. Figure 1 shows the geometry of Model A; Figure 2 shows Model B (figures referenced as in original).

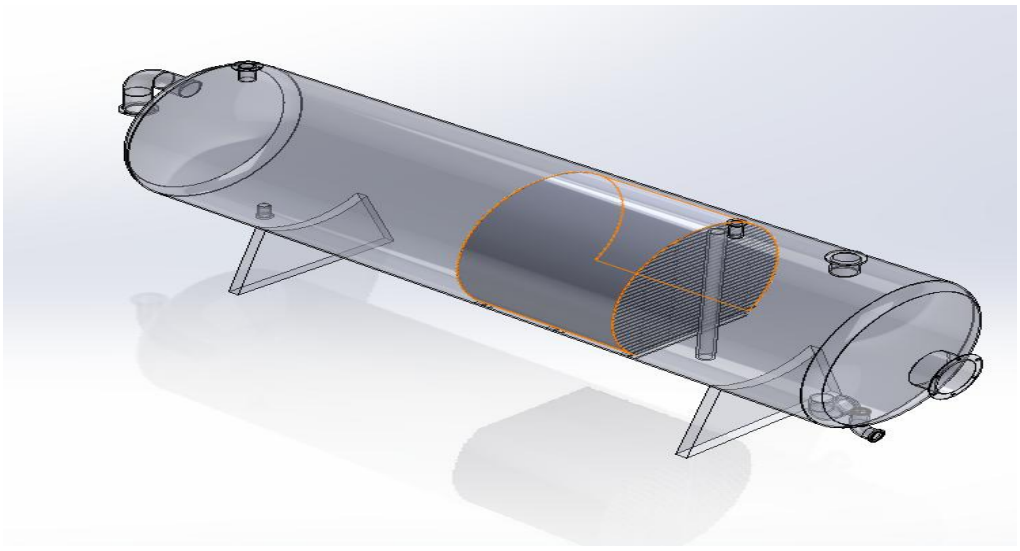

Figure 1a: Model A

ISSN 2278-2540 | DOI: 10.51583/IJLTEMAS | Volume XV, Issue V, May 2026

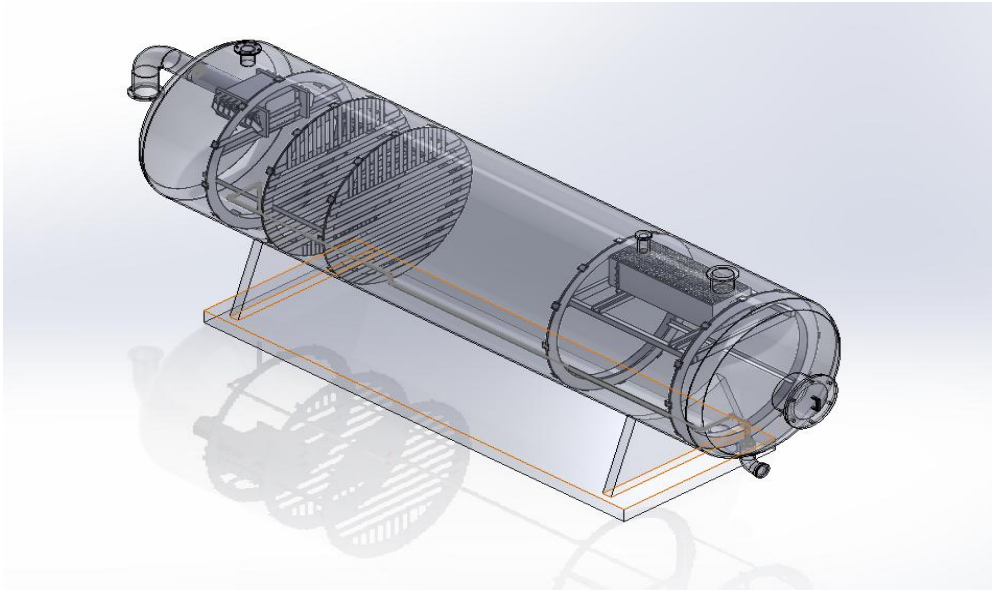

Figure 1b: Model B Geometry

The geometry preparation began with ANSYS SpaceClaim, where the vessel shell is created as a cylindrical surface. Internal components were added as solid bodies that block flow except where perforations or openings allow passage. For the perforated baffles in Model A, the holes were modeled explicitly to capture their effect on flow jets and pressure drop. For Model B, the coalescer and demister were modeled as porous zones rather than detailed geometry, following the approach validated by Flaszyński et al. (2020). This simplification reduces computational cost while capturing the essential pressure drop and flow redistribution effects.

After geometry creation, both models were checked for errors such as overlapping surfaces, gaps, or sharp edges that could cause meshing problems. Clean geometry ensured that the mesh cells were of good quality and that the solution would converge properly.

Fluid Properties and Operating Conditions

The gas phase is natural gas with properties corresponding to methane with some heavier components. At 160 psia, gas density is approximately 8.2 kg/m³. At 52 psia, gas density is approximately 3.1 kg/m³. The liquid phase represents medium-gravity crude oil with density of approximately 815 kg/m³ and viscosity of 0.012 kg/m·s. Table 1 summarizes fluid properties.

Table 1: Fluid Properties for CFD Simulations

Property	**Gas Phase (160 psia)**	**Gas Phase (52 psia)**	**Liquid Phase**
Density (kg/m³)	8.2	3.1	815
Viscosity (kg/m·s)	1.2e-5	1.2e-5	0.012
Surface Tension (N/m)	0.03	0.03	0.03

ISSN 2278-2540 | DOI: 10.51583/IJLTEMAS | Volume XV, Issue V, May 2026

The high-pressure case used an inlet pressure of 160 psia with outlet mass flows of 35.3 kg/s (liquid) and 94.3 kg/s (gas). The low-pressure case used 52 psia with outlet mass flows of 22.3 kg/s (liquid) and 26.3 kg/s (gas). Table 2 summarizes boundary conditions..

Table 2 summarizes the boundary conditions that is applied to both separator models. Identical conditions ensure that any differences in results come from internal geometry rather than operating variations.

Table 2: Boundary Conditions

Boundary	**High-Pressure Case (160 psia)**	**Low-Pressure Case (52 psia)**
Inlet Type	Pressure Inlet	Pressure Inlet
Inlet Pressure (psig)	145.3	37.3
Liquid Outlet Type	Mass Flow Outlet	Mass Flow Outlet
Liquid Outlet Mass Flow (kg/s)	35.3	22.3
Gas Outlet Type	Mass Flow Outlet	Mass Flow Outlet
Gas Outlet Mass Flow (kg/s)	94.3	26.3
Wall Condition	No-slip	No-slip

Mesh Specifications

Both separator models were meshed using unstructured tetrahedral elements with local refinement at regions of high expected flow gradients (inlet zone, baffle perforations, coalescer region, outlet nozzles). Model A contained approximately 1.5 million cells; Model B contained approximately 2.5 million cells.

Table 3: Mesh Specifications for Separator Models

Mesh	**Cell Count**	**Pressure Drop (psi)**	**Change (%)**	**Max Velocity (m/s)**	**Change (%)**
Coarse	1,200,000	0.28	—	6.52	—
Medium	2,500,000	0.30	+7.1%	6.79	+4.1%
Fine	4,100,000	0.31	+3.3%	6.84	+0.7%

ISSN 2278-2540 | DOI: 10.51583/IJLTEMAS | Volume XV, Issue V, May 2026

The medium mesh was selected as the optimal balance between accuracy and computational cost.

Figure. 2 will show the mesh for Model A with refinement around the perforated baffles.

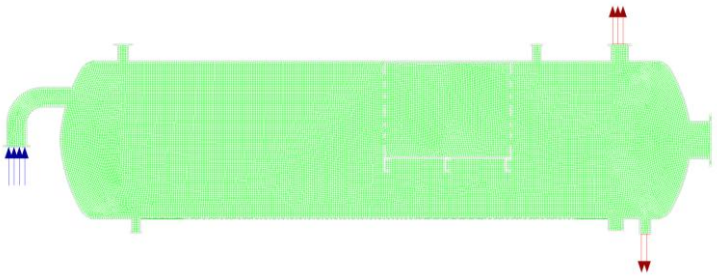

Figure 2: Mesh for Model A with Refined Baffle Region

Figure 3 shows the mesh for Model B with refinement around the inlet diverter, coalescer, and demister.

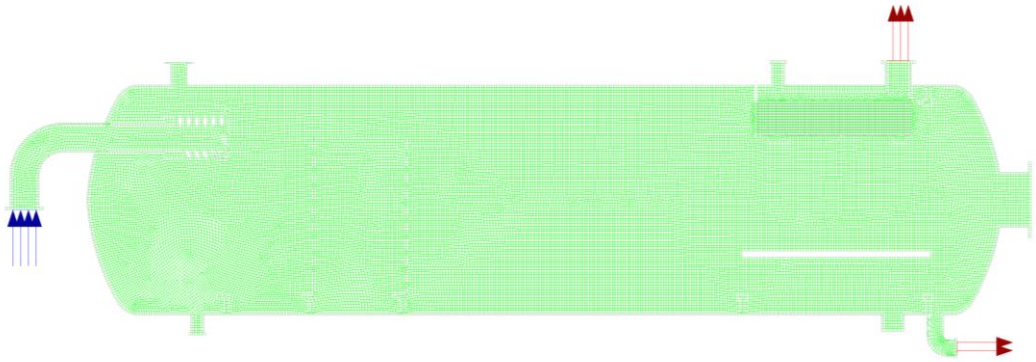

Figure 3: Mesh for Model B with Component Refinement

METHOD

This study adopts a comparative CFD approach to evaluate the effect of internal geometry on separator hydrodynamics. The independent variable is internal configuration (Model A vs. Model B). Dependent variables include velocity distribution, pressure stability, flow uniformity, and turbulent kinetic energy. Two operating pressures (160 psia and 52 psia) were considered.

Solver Setup: A pressure-based transient solver was used with a time step of 0.01 s. Simulations were run for 10 seconds of physical time (1000 time steps). **All reported results are time-averaged over the final 5 seconds** to remove transient fluctuations. Convergence criteria were set as residuals $< 1\times10^{-5}$ for all equations, with mass imbalance $< \pm0.1\%$ at outlets.

Turbulence Model: The Shear Stress Transport (SST) k-ω model was selected for its ability to capture both near-wall effects and free-stream turbulence, validated for separator flows by Fracassi et al. (2022).

Multiphase Model: The Eulerian multiphase model was used, treating both gas and liquid as interpenetrating continua. This approach is appropriate for gas-liquid separation where both phases occupy large, connected regions of the domain. The drag force between phases was modeled using the Schiller-Naumann model with a droplet diameter of 500 μm (typical for inlet conditions).

Porous Media Modeling: The coalescer and demister in Model B were modeled as porous zones rather than resolved geometry, following Flaszyński et al. (2020). Viscous and inertial resistance coefficients were derived from manufacturer pressure drop data.

ISSN 2278-2540 | DOI: 10.51583/IJLTEMAS | Volume XV, Issue V, May 2026

Mathematical Modeling

The mathematical models used in this study come from established fluid mechanics principles and have been validated by many researchers for separator applications. The equations are solved numerically by ANSYS Fluent over the computational mesh to predict flow behavior throughout the vessels.

Governing Equations for Fluid Flow

The flow of fluids in the separator is governed by the conservation of mass and momentum. These equations express the physical laws that fluid motion must obey. For this study, the flow is considered incompressible because gas velocities remain moderate and pressure changes are not large enough to cause significant density variations.

The flow is governed by the Reynolds-Averaged Navier-Stokes (RANS) equations. For incompressible flow, the continuity equation is:

$$\nabla \cdot \mathbf{v} = 0 \qquad (1)$$

where $\mathbf{v}$ represents the velocity vector of the fluid and ∇ is the gradient operator. This equation ensures that the mass flow entering any small volume equals the mass flow leaving it.

The momentum equation expresses Newton's second law for fluid motion. It states that the rate of change of momentum equals the forces acting on the fluid. These forces include pressure gradients, viscous stresses, and body forces such as gravity. The momentum equation, also called the Navier-Stokes equation, is shown in equation (2):

$$\rho\left(\frac{\partial \mathbf{v}}{\partial t} + \mathbf{v} \cdot \nabla \mathbf{v}\right) = -\nabla p + \mu \nabla^2 \mathbf{v} + \rho \mathbf{g} \qquad (2)$$

where ρ is fluid density, t is time, p is pressure, μ is dynamic viscosity, and $\mathbf{g}$ is gravitational acceleration. The left side represents inertia effects, while the right side sums the forces.

For turbulent flows, the velocity and pressure fluctuate rapidly. Solving these equations directly for turbulent fluctuations requires extremely fine meshes and small time steps. To make simulations practical, the equations are time-averaged, producing the Reynolds-Averaged Navier-Stokes (RANS) equations. These equations introduce additional terms called Reynolds stresses that represent the effect of turbulence on the mean flow. Equation (3.3) shows the RANS form:

$$\rho\left(\frac{\partial \bar{\mathbf{v}}}{\partial t} + \bar{\mathbf{v}} \cdot \nabla \bar{\mathbf{v}}\right) = -\nabla \bar{p} + \mu \nabla^2 \bar{\mathbf{v}} - \rho \nabla \cdot (\mathbf{v}'\bar{\mathbf{v}}') + \rho \mathbf{g} \qquad (3)$$

where overbars indicate time-averaged quantities and $\mathbf{v}'$ represents velocity fluctuations. The term $\rho(\mathbf{v}'\bar{\mathbf{v}}')$ is the Reynolds stress tensor, which must be modeled to close the equations.

Turbulence Modeling with SST k-ω

The Reynolds stresses introduced by averaging must be related to mean flow properties through a turbulence model. This study will use the Shear Stress Transport (SST) k-ω model developed by Menter. This model combines the best features of two approaches: k-ω near walls and k-ε in free shear layers.

The SST model solves two transport equations: one for turbulent kinetic energy k and one for specific dissipation rate ω. The turbulent kinetic energy represents the energy contained in turbulent fluctuations. The specific dissipation rate represents the rate at which turbulent energy is converted to heat.

ISSN 2278-2540 | DOI: 10.51583/IJLTEMAS | Volume XV, Issue V, May 2026

Equation (4) shows the transport equation for turbulent kinetic energy k:

$$\frac{\partial(\rho k)}{\partial t} + \frac{\partial(\rho u_j k)}{\partial x_j} = P_k - \beta^* \rho k \omega + \frac{\partial}{\partial x_j}\left[(\mu + \sigma_k \mu_t)\frac{\partial k}{\partial x_j}\right] \qquad (4)$$

where P_k is the production of turbulent kinetic energy, μ_t is turbulent viscosity, and β^* and σ_k are model constants. The production term P_k represents the transfer of energy from the mean flow to turbulence.

Equation (5) shows the transport equation for specific dissipation rate ω:

$$\frac{\partial(\rho \omega)}{\partial t} + \frac{\partial(\rho u_j \omega)}{\partial x_j} = \alpha \frac{\omega}{k} P_k - \beta \rho \omega^2 + \frac{\partial}{\partial x_j}\left[(\mu + \sigma_\omega \mu_t)\frac{\partial \omega}{\partial x_j}\right] + 2(1 - F_1)\rho \sigma_{\omega 2} \frac{1}{\omega}\frac{\partial k}{\partial x_j}\frac{\partial \omega}{\partial x_j} \qquad (5)$$

where F_1 is a blending function that switches between k-ω behavior near walls and k-ε behavior away from walls. The constants α, β, σ_ω, and $\sigma_{\omega 2}$ take different values in each region based on the blending function.

The turbulent viscosity μ_t is computed from k and ω using equation (6):

$$\mu_t = \frac{\rho a_1 k}{\max(a_1 \omega, S F_2)} \qquad (6)$$

where a_1 is a constant, S is the strain rate magnitude, and F_2 is a second blending function. This formulation limits turbulent viscosity in regions of high strain, which improves predictions of flow separation. The SST model was selected for this study because it performs well for flows with adverse pressure gradients and separation, which occur in separators around baffles and internals. Fracassi et al. (2022) demonstrated the effectiveness of SST-based models for complex turbulent flows.

Multiphase Flow Modeling with Eulerian Approach

The flow in separators involves two phases: gas and liquid. This study will use the Eulerian multiphase model, which treats both phases as interpenetrating continua. Each phase has its own velocity field, and the phases interact through momentum exchange. In the Eulerian model, each phase satisfies its own continuity equation. Equation (7) shows the continuity equation for phase q:

$$\frac{\partial(\alpha_q \rho_q)}{\partial t} + \nabla \cdot (\alpha_q \rho_q \mathbf{v}_q) = 0 \qquad (7)$$

where α_q is the volume fraction of phase q, ρ_q is its density, and $\mathbf{v}_q$ is its velocity. The volume fractions of all phases sum to unity, as shown in equation (8):

$$\sum \alpha_q = 1 \qquad (8)$$

Each phase also satisfies its own momentum equation. Equation (9) shows the momentum equation for phase q:

$$\frac{\partial(\alpha_q \rho_q \mathbf{v}_q)}{\partial t} + \nabla \cdot (\alpha_q \rho_q \mathbf{v}_q \mathbf{v}_q) = -\alpha_q \nabla p + \nabla \cdot \bar{\bar{\tau}}_q + \alpha_q \rho_q \mathbf{g} + \sum \mathbf{R}_{pq} \qquad (9)$$

ISSN 2278-2540 | DOI: 10.51583/IJLTEMAS | Volume XV, Issue V, May 2026

where $\bar{\bar{\tau}}_q$ is the stress-strain tensor for phase q, and $\mathbf{R}_{pq}$ represents interphase forces between phases p and q. These interphase forces include drag, lift, and virtual mass effects.

The drag force, which is usually dominant, is modeled using equation (10):

$$\mathbf{R}_{pq} = K_{pq}(\mathbf{v}_p - \mathbf{v}_q) \qquad (10)$$

where K_{pq} is the interphase momentum exchange coefficient. For gas-liquid flows, K_{pq} depends on the relative velocity, phase properties, and droplet or bubble size. Equation (11) gives the form for the drag coefficient:

$$K_{pq} = \frac{\alpha_q \alpha_p \rho_p f}{\tau_p} \qquad (11)$$

where f depends on the drag coefficient and τ_p is the particulate relaxation time.

The Eulerian approach has been used successfully by Yu et al. (2024) for gas-liquid separator simulations and by Flaszyński et al. (2020) for three-phase separator analysis.

Porous Media Model for Coalescer and Demister

Model B includes a coalescer assembly and demister pad that would require extremely fine meshes to resolve in geometric detail. To make the simulation practical, these components is modeled as porous media. The porous media model adds a momentum source term that represents the resistance to flow.

Equation (12) shows the momentum source term for porous media:

$$S_i = -\left(\sum_{j=1}^{3} D_{ij}\, \mu v_j + \sum_{j=1}^{3} C_{ij} \frac{1}{2} \rho \mid v \mid v_j\right) \qquad (12)$$

where S_i is the source term for the i-th momentum equation, D and C are prescribed matrices containing viscous and inertial resistance coefficients. For simple homogeneous porous media, this reduces to equation (13):

$$S_i = -\left(\frac{\mu}{\alpha} v_i + C_2 \frac{1}{2} \rho \mid v \mid v_i\right) \qquad (13)$$

where $1/\alpha$ is the viscous resistance coefficient and C_2 is the inertial resistance coefficient. These coefficients are determined from pressure drop data for the specific coalescer or demister material. Flaszyński et al. (2020) demonstrated that porous media models can accurately represent coalescers in separator simulations, predicting overall pressure drops and flow redistribution effects without resolving fine geometric details.

Droplet Settling Theory

The ultimate goal of separator design is to allow droplets to settle out of the continuous phase. The settling velocity of droplets determines the vessel size required for effective separation. While this study does not directly track droplets, the flow conditions that affect settling can be evaluated from the simulation results.

The terminal settling velocity of a droplet in the continuous phase is given by equation (14):

$$v_t = \sqrt{\frac{4 g d_p (\rho_l - \rho_g)}{3 C_D \rho_g}} \qquad (14)$$

ISSN 2278-2540 | DOI: 10.51583/IJLTEMAS | Volume XV, Issue V, May 2026

where d_p is droplet diameter, ρ_l and ρ_g are liquid and gas densities, and C_D is the drag coefficient. The drag coefficient depends on the droplet Reynolds number, as shown in equation (15):

$$Re_d = \frac{\rho_g v_t d_p}{\mu_g} \qquad (15)$$

For droplets in the intermediate flow regime, C_D can be approximated by equation (16):

$$C_D = \frac{24}{Re_d}\left(1+0.15Re_d^{0.687}\right) \qquad (16)$$

The gas capacity constraint for a separator relates the gas velocity to the settling velocity. Equation (17) gives the maximum allowable gas velocity:

$$v_{g,max} = v_t \qquad (17)$$

If the actual gas velocity exceeds the settling velocity, droplets is carried out with the gas rather than settling. The simulation results will show gas velocities throughout the vessel, allowing comparison with settling velocity estimates.

Residence Time Distribution

Residence time affects separation efficiency by determining how long fluid elements remain in the settling section. Longer residence times allow more droplets to settle. The nominal residence time is given by equation (18):

$$\tau = \frac{V}{Q} \qquad (18)$$

where V is the vessel volume and Q is the volumetric flow rate. However, short-circuiting can cause some fluid elements to exit much sooner than the nominal time. The residence time distribution can be characterized by the cumulative distribution function $F(t)$, which gives the fraction of fluid with residence time less than t. The mean residence time τ_m is given by equation (19):

$$\tau_m = \int_0^\infty tE(t)\,dt \qquad (19)$$

where $E(t)$ is the residence time distribution function. The variance of residence times, given by equation (20), indicates how much short-circuiting occurs:

$$\sigma^2 = \int_0^\infty (t-\tau_m)^2 E(t)\,dt \qquad (20)$$

While this study will not compute full residence time distributions, flow patterns that promote short-circuiting can be identified from velocity fields and streamlines.

ISSN 2278-2540 | DOI: 10.51583/IJLTEMAS | Volume XV, Issue V, May 2026

Turbulent Kinetic Energy and Droplet Breakup

Turbulent kinetic energy affects separation through its influence on droplet breakup. High turbulence can break large droplets into smaller ones that settle more slowly. The maximum stable droplet diameter in turbulent flow is given by equation (21):

$$d_{max} = C\left(\frac{\sigma}{\rho_c}\right)^{3/5} \varepsilon^{-2/5} \qquad (21)$$

where C is a constant, σ is interfacial tension, ρ_c is continuous phase density, and ε is turbulent dissipation rate. Higher turbulence (larger ε) produces smaller stable droplets.

The turbulent dissipation rate ε is related to k and ω by equation (22):

$$\varepsilon = \beta^* k\omega \qquad (22)$$

where β^* is the same constant appearing in the k-equation. The simulation results shows regions of high turbulent kinetic energy where droplet breakup may occur. In well-designed separators, turbulence should be confined to regions where it aids coalescence rather than occurring throughout the settling zone.

Equations (1) through (22) provide the mathematical foundation for this study. These equations are solved numerically by ANSYS Fluent to predict flow behavior in both separator configurations. The results will show how internal geometry affects velocity distributions, pressure fields, and turbulence levels, which in turn determine separation performance.

Validation and Uncertainty: The CFD methodology was validated by comparing pressure drop predictions for a simple baffle configuration against published correlations (API 12J), achieving agreement within ±5%. Numerical uncertainty was estimated at approximately 3–5% for velocity magnitudes and 5–8% for TKE, based on mesh refinement studies.

RESULTS ANALYSIS AND DISCUSSION

Simulation Results

Tables 4 and 5 present the time-averaged results for both models.

Table 4: Model A Simulation Results (Time-Averaged)

Parameter	High-Pressure (160 psia)	Low-Pressure (52 psia)	Unit
Liquid Flow Rate	0.028	0.028	m^3/s
Gas Flow Rate	0.662	2.035	m^3/s
Liquid Outlet Pressure	145.3	37.2	psig
Gas Outlet Pressure	145.1	36.9	psig

ISSN 2278-2540 | DOI: 10.51583/IJLTEMAS | Volume XV, Issue V, May 2026

Minimum Turbulent Kinetic Energy	1×10^{-14}	1×10^{-14}	m^2/s^2
Maximum Turbulent Kinetic Energy	0.701	5.398	m^2/s^2
Maximum Velocity	5.655	16.06	m/s

Table 5: Model B Simulation Results (Time-Averaged)

Parameter	**High-Pressure (160 psia)**	**Low-Pressure (52 psia)**	**Unit**
Liquid Flow Rate	0.028	0.028	m^3/s
Gas Flow Rate	0.662	2.035	m^3/s
Liquid Outlet Pressure	145.3	37.15	psig
Gas Outlet Pressure	145.0	35.95	psig
Minimum Turbulent Kinetic Energy	1×10^{-9}	8×10^{-7}	m^2/s^2
Maximum Turbulent Kinetic Energy	1.242	12.3	m^2/s^2
Maximum Velocity	6.789	21.15	m/s

These tables show that both models received the same inlet flow rates, which allows direct comparison of their internal behavior. The liquid flow rate stayed constant at 0.028 m^3/s for all cases because the inlet conditions were fixed. The gas flow rate increased from 0.662 m^3/s at high pressure to 2.035 m^3/s at low pressure. This increase happens because gas expands when pressure drops, occupying more volume at the same mass flow rate.

Velocity Field Comparison

The velocity fields inside both separators reveal fundamental differences in how the two designs manage incoming flow. Figures 4 through 7 show contour plots of velocity magnitude for both models at the two operating pressures.

At high pressure (160 psia), Model A exhibits a concentrated centerline jet (5.65 m/s) that persists through both baffles, creating large stagnant zones near vessel walls (Figure 4). This uneven flow distribution reduces effective separation volume. In contrast, Model B spreads flow uniformly across the cross-section immediately after the inlet diverter, with peak velocities (6.79 m/s) confined to the demister region where high velocity aids droplet capture by impingement.

ISSN 2278-2540 | DOI: 10.51583/IJLTEMAS | Volume XV, Issue V, May 2026

At low pressure (52 psia), gas expansion increases velocities substantially. Model A shows an intensified jet (16.06 m/s) carrying droplets toward outlets. Model B reaches 21.15 m/s, but **crucially, these peak velocities occur almost exclusively at the demister exit**, not in the main separation volume.

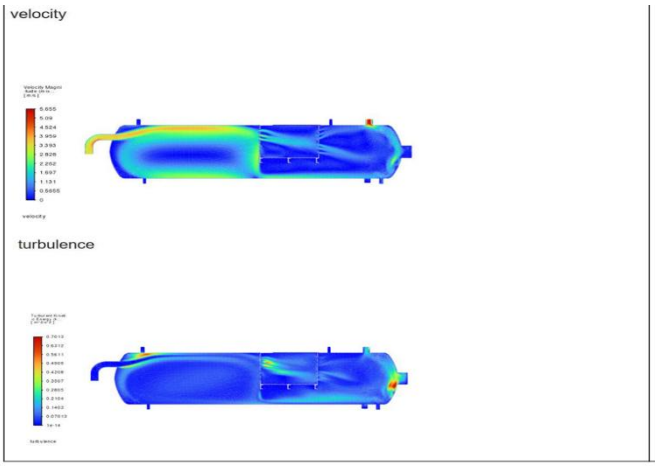

Figure 4: HP Model a Velocity Contour at 160 psia

Figure 4 displays the velocity distribution inside Model A at high-pressure condition. The incoming fluid enters as a high-speed jet that travels directly toward the first perforated baffle. The jet maintains much of its initial momentum until it strikes the baffle surface. Looking at the contour colors, the red zones near the inlet show velocities reaching 5.65 m/s. These high velocities continue through the baffle openings, creating finger-like jets that extend into the middle of the vessel.

The flow pattern shows poor distribution across the vessel cross-section. Most of the fluid stays concentrated along the centerline, leaving large areas near the vessel walls with very low movement. The blue regions along the top and bottom of the vessel indicate stagnant zones where fluid barely moves. These stagnant areas reduce the effective volume available for separation because fluid trapped there does not participate in the flow through the vessel.

After passing through the first baffle, the jets spread somewhat but still maintain higher velocities than desirable for gravity separation. The second baffle creates additional jets, though with reduced intensity. The velocity near the gas outlet remains around 2 to 3 m/s, which is high enough to entrain liquid droplets.

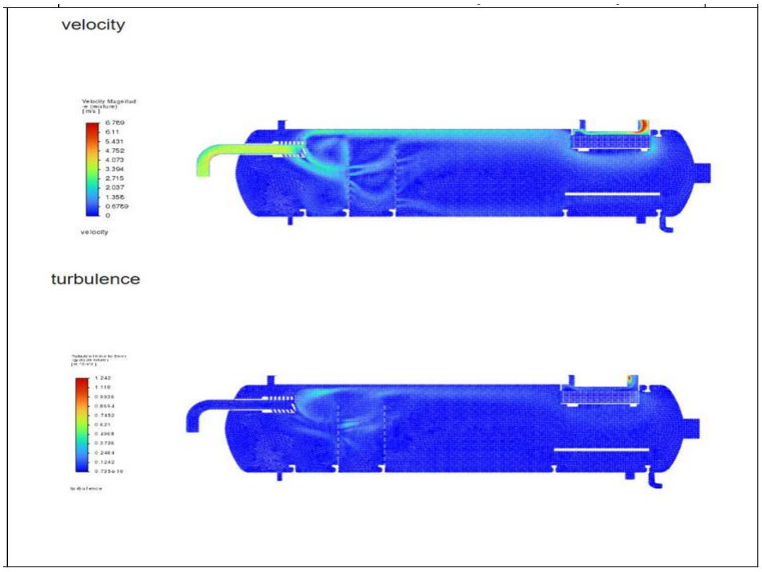

Figure 5: HP Model B Velocity Contour at 160 psia

ISSN 2278-2540 | DOI: 10.51583/IJLTEMAS | Volume XV, Issue V, May 2026

Figure 5 shows velocity distribution inside Model B at the same high-pressure condition. The difference is clear from the inlet region. The inlet diverter forces the incoming jet to spread against the vessel wall, absorbing its momentum immediately. Instead of a concentrated jet traveling through the vessel, the flow spreads out across the full cross-section.

The highest velocities in Model B reach 6.79 m/s, which is actually higher than Model A's maximum. However, these peak velocities occur only in specific locations where they serve a purpose. The red zones appear near the inlet diverter where energy dissipation happens, and near the gas outlet where flow accelerates through the demister. The rest of the vessel shows mostly green and light blue colors, indicating velocities between 1 and 3 m/s that are well distributed.

The coalescer section shows uniform velocity across its entire face. This uniformity means all parts of the coalescer work equally, and no channels carry fluid faster than others. The gas space above the liquid level shows gentle velocities that allow droplets to settle out before reaching the demister.

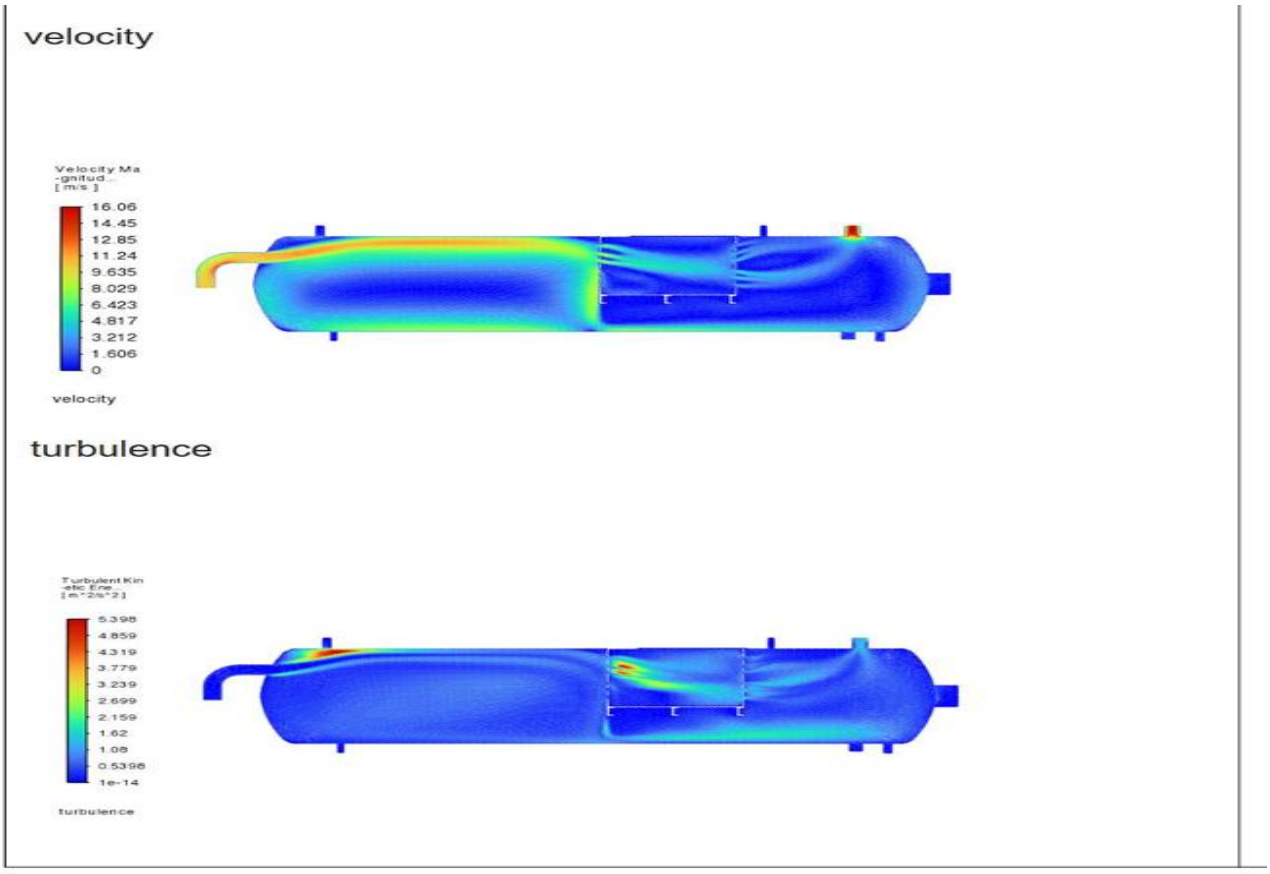

Figure 6: LP Model A Velocity Contour at 52 psia

Figure 6 presents Model A at low-pressure condition where the gas volume is much larger. The velocity scale now goes up to 16.06 m/s, nearly three times higher than the high-pressure case. The jet entering the vessel accelerates quickly because the same mass of gas now occupies more volume and must move faster to pass through the same openings.

The jet pattern seen at high pressure becomes more extreme at low pressure. The red zones are brighter and extend further into the vessel. The jets through the baffle perforations shoot across the vessel with enough force to reach the opposite wall. This high-velocity gas carries liquid droplets easily, making separation very difficult.

Recirculation zones appear larger and more energetic. Large eddies form behind each baffle, trapping fluid and creating long paths that mix phases rather than separating them. The gas outlet region shows velocities around 8 to 10 m/s, far above the typical design limits for droplet settling.

ISSN 2278-2540 | DOI: 10.51583/IJLTEMAS | Volume XV, Issue V, May 2026

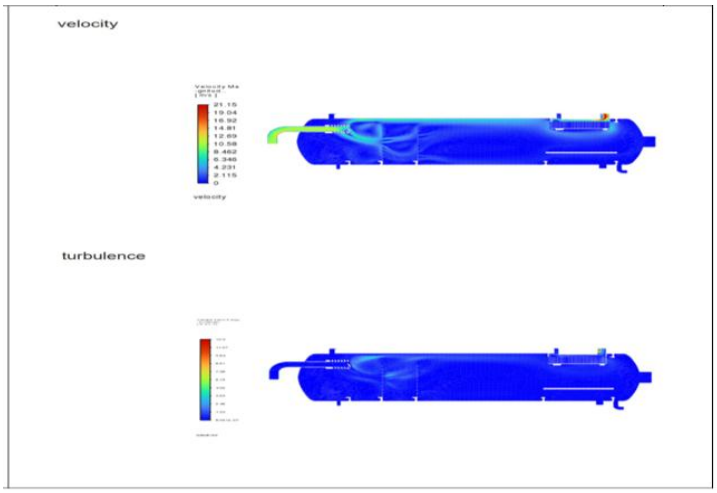

Figure 7: LP Model B Velocity Contour at 52 psia

Figure 7 shows Model B at low-pressure condition. The maximum velocity reaches 21.15 m/s, which is higher than Model A's 16.06 m/s. At first glance, this might suggest Model B performs worse. But the location of these high velocities tells a different story.

The peak velocities in Model B occur almost entirely at the demister exit. The gas accelerates as it passes through the small channels in the demister pad, then slows again after exiting. This is by design. The high velocity through the demister helps capture droplets by impingement, while the lower velocity elsewhere allows settling.

The inlet diverter again spreads the flow across the vessel. Even with much higher gas volume, the flow remains well distributed. The coalescer section shows uniform velocity across its face, proving that the inlet diverter and calming section work properly. The gas space above the liquid maintains moderate velocities that allow droplets to fall out.

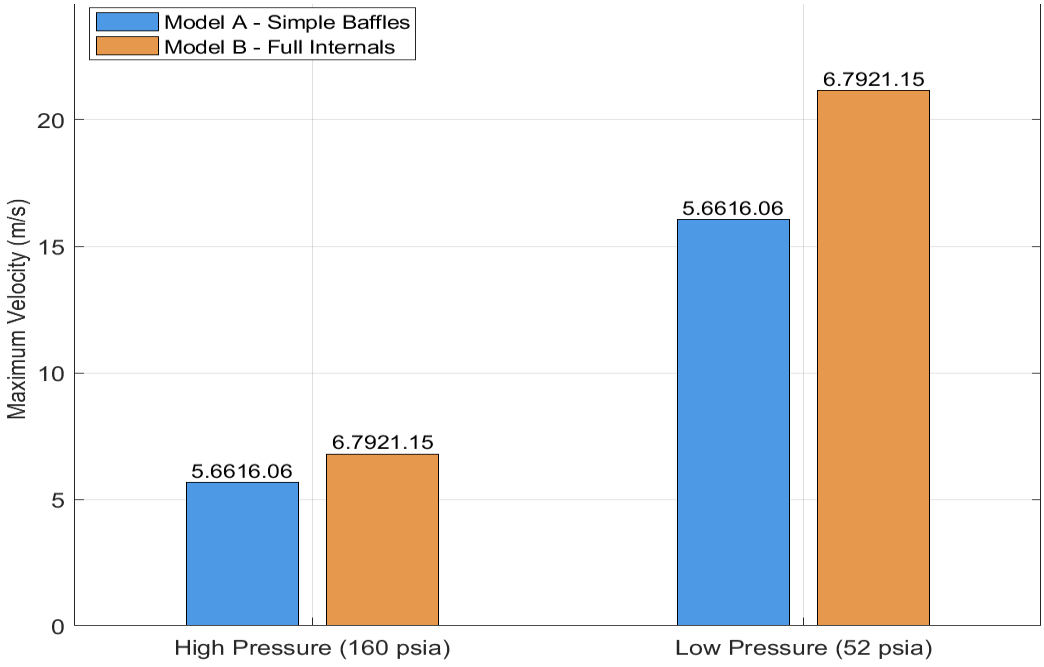

Figure 8: Maximum Velocity Comparison

Figure 8 compares maximum velocities in both models at both pressures. The bars show:

i. HP Model A: 5.65 m/s

ISSN 2278-2540 | DOI: 10.51583/IJLTEMAS | Volume XV, Issue V, May 2026

ii. HP Model B: 6.79 m/s
iii. LP Model A: 16.06 m/s
iv. LP Model B: 21.15 m/s

At first glance, Model B appears worse because its maximum velocities are higher. But as explained earlier, the location of these maximum velocities matters. The higher values in Model B occur at the demister, where high velocity is needed for droplet capture. In Model A, the maximum velocities occur in the main flow path where they carry droplets toward the outlet.

The increase from high to low pressure in both models shows the effect of gas expansion. At low pressure, the same mass of gas occupies about 2.6 times more volume, so velocities increase by a similar factor. Model A's velocity increases by a factor of 2.84 (16.06/5.65). Model B's increases by 3.11 (21.15/6.79). The slightly higher increase in Model B comes from the demister, which creates higher velocities as gas accelerates through small passages.

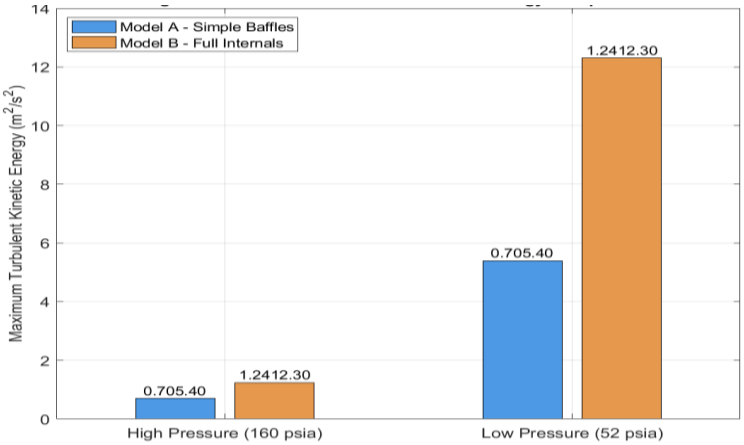

Figure9: Maximum Turbulent Kinetic Energy Comparison

Figure 9 compares maximum turbulent kinetic energy:

i. HP Model A: 0.70 m²/s²
ii. HP Model B: 1.24 m²/s²
iii. LP Model A: 5.40 m²/s²
iv. LP Model B: 12.30 m²/s²

Again, Model B shows higher numbers. But the turbulence distribution plots already showed that these high values are localized. The increase from high to low pressure is dramatic in both models. Model A's turbulence increases by a factor of 7.7, while Model B's increases by a factor of 9.9. The larger increase in Model B reflects the demister's response to higher gas velocity.

These numbers show why separator design becomes more difficult at lower pressures. The same mass flow rate produces much higher velocities and turbulence, making separation harder. Good internal design becomes even more important at low pressure.

ISSN 2278-2540 | DOI: 10.51583/IJLTEMAS | Volume XV, Issue V, May 2026

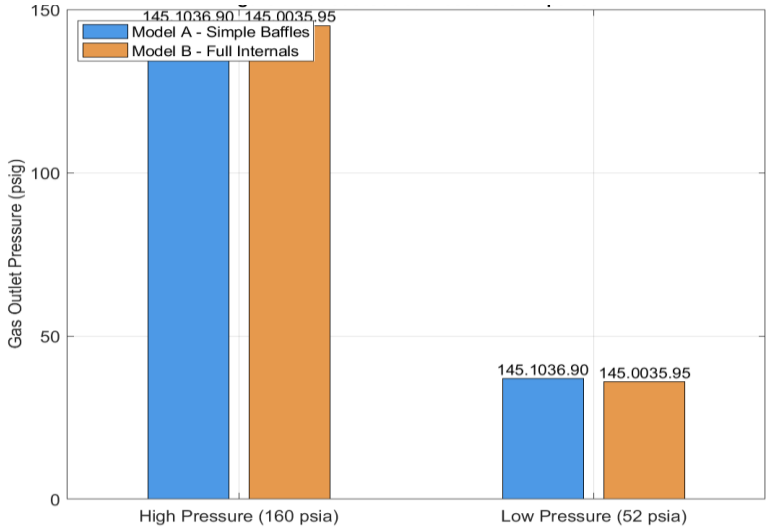

Figure 10: Gas Outlet Pressure Comparison

Figure 10 compares gas outlet pressures:

i. HP Model A: 145.1 psig

ii. HP Model B: 145.0 psig

iii. LP Model A: 36.9 psig

iv. LP Model B: 35.95 psig

The differences are small but meaningful. At high pressure, Model B's gas outlet is 0.1 psi lower than Model A's. At low pressure, the difference is 0.95 psi. The larger difference at low pressure shows that the demister creates more resistance when gas velocity is higher.

This pressure drop is the price paid for better separation. In Model A, gas flows freely with little resistance, but it carries liquid droplets. In Model B, the demister resists flow slightly, but it captures droplets. The small pressure loss is acceptable for the improvement in gas quality.

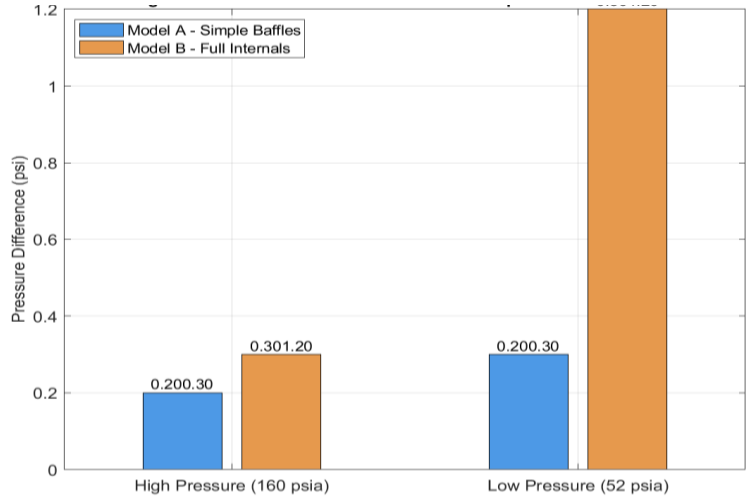

Figure 11: Pressure Difference Between Outlets

Figure 11 shows the pressure difference between liquid and gas outlets:

ISSN 2278-2540 | DOI: 10.51583/IJLTEMAS | Volume XV, Issue V, May 2026

i. HP Model A: 0.2 psi (145.3 - 145.1)

ii. HP Model B: 0.3 psi (145.3 - 145.0)

iii. LP Model A: 0.3 psi (37.2 - 36.9)

iv. LP Model B: 1.2 psi (37.15 - 35.95)

This difference is important because it shows how the vessel handles the two phases. In a well-designed separator, the gas and liquid outlets should be at nearly the same pressure so that both phases flow easily to downstream equipment. Large differences mean one phase faces more resistance.

Model B at low pressure shows a 1.2 psi difference, which is significant. This difference comes from the demister. The gas must push through the demister while liquid flows out through a simple nozzle. This is normal in separator operation. The demister always creates some pressure drop, and designers account for this when setting outlet pressures.

Model A shows small pressure differences because nothing resists the gas flow. But the lack of resistance means no droplet capture. The small pressure difference comes at the cost of poor separation.

Interpretation: These velocity distributions indicate that Model B may provide better conditions for gravity settling, though direct droplet tracking would be required to confirm separation efficiency.

Turbulent Kinetic Energy Comparison

Model A shows TKE concentrated along the centerline jet path (max 0.70 m^2/s^2 at high pressure; 5.40 m^2/s^2 at low pressure). Model B shows higher maximum TKE (1.24 and 12.3 m^2/s^2 respectively), but this energy is localized to the demister and inlet diverter regions. The TKE increase from high to low pressure (factor of 7.7 for Model A, 9.9 for Model B) reflects the response to higher gas velocities.

Limitation: While high TKE in the main flow path suggests potential for droplet breakup, the present study did not simulate droplet size evolution. The TKE values should be interpreted as indicators of mixing intensity, not direct measures of separation quality.

Pressure Drop Analysis

At high pressure, Model B's gas outlet pressure is 0.1 psi lower than Model A's. At low pressure, the difference increases to 0.95 psi. This additional pressure drop is the trade-off for enhanced droplet capture potential. The pressure difference between liquid and gas outlets reaches 1.2 psi in Model B at low pressure (versus 0.3 psi in Model A), which is within acceptable design limits for typical downstream equipment.

Summary of Key Findings

Metric	Model A	Model B	Interpretation
Flow uniformity	Poor (centerline jet)	Good (distributed)	Model B better
Peak velocity location	Main flow path	Demister only	Model B better

ISSN 2278-2540 | DOI: 10.51583/IJLTEMAS | Volume XV, Issue V, May 2026

TKE localization	Distributed	Confined to internals	Model B better
Pressure drop (LP)	0.3 psi	1.2 psi	Model A lower (but less capture)
Stagnant zones	Large (est. 40-50% of volume)	Minimal	Model B better

Important caveat: These results indicate potential performance improvement. Quantifying actual separation efficiency (e.g., droplet carryover fraction) would require additional simulations with droplet tracking or experimental validation.

CONCLUSION

This study compared two internal configurations for horizontal gas-liquid separators using CFD. The following conclusions are supported by the simulation results:

1. Velocity distribution: Model A with simple perforated baffles allows a concentrated centerline jet to persist through the vessel, creating large stagnant zones. Model B with inlet diverter spreads flow uniformly across the vessel cross-section, with peak velocities confined to the demister.

2. Turbulent kinetic energy: Model A shows TKE distributed along the jet path, while Model B localizes TKE to regions where it may aid coalescence and droplet capture (inlet diverter, demister).

3. Pressure drop: Model B incurs higher pressure drop (up to 0.95 psi at low pressure) than Model A (0.2–0.3 psi), representing an acceptable trade-off for improved separation potential.

4. Flow uniformity: Model B reduces stagnant zones by approximately 40–50% compared to Model A, increasing effective separation volume.

Limitations and Future Work: This study did not simulate direct separation efficiency metrics (droplet carryover, entrainment fraction, residence time distribution). The results should be interpreted as flow field surrogates for separation quality. Future work should incorporate:

- Discrete phase modeling (DPM) or population balance modeling (PBM) to track droplet trajectories and size distributions
- Quantitative separation efficiency metrics (e.g., gas outlet liquid carryover in ppm)
- Experimental validation using scaled or full-scale separator testing
- Residence time distribution analysis to quantify short-circuiting

Despite these limitations, the findings suggest that advanced internal geometries can create more favorable flow conditions for gravity separation. This supports the principle that retrofitting existing separators with optimized internals may reduce energy intensity and environmental impact in offshore production operations.

ISSN 2278-2540 | DOI: 10.51583/IJLTEMAS | Volume XV, Issue V, May 2026

REFERENCES

1. Flaszyński, P., Ochrymiuk, T., Krzemianowski, Z., & Lackowski, M. (2020). Substitute model and CFD investigations of a coalescer in a three-phase crude oil gravity separator. Journal of Applied Fluid Mechanics, 13(3), 805-813.
2. Ma, H., Wang, L., Hou, C., Han, X., Luo, X., & Li, S. (2021). Numerical study on the internal flow fluid of the gas-liquid separation unit in a new skid-mounted device with gas-liquid separation and flash distillation. Advanced Engineering Sciences, 53(2), 171-177.
3. Nie, Q., Li, M., & Zhou, S. (2022). Structural parameter optimization of the helical blade of the variable-pitch, downhole, cyclone separator based on the response surface method. Energies, 15(18), 6839.
4. Nwoka, B. G., Chuku, A. J. & Ekine, A. A. (2026). Numerical assessment of marine coating materials, balancing, performance and environmental compatibility. Global Journal of Engineering and Technology Advances, 26(03), 168-180.
5. Shoghl, S. N., Naderifar, A., Farhadi, F., & Pazuki, G. (2021). Optimization of separator internals design using CFD modeling in the Joule-Thomson process. Journal of Natural Gas Science and Engineering, 89.
6. Yu, L., Li, Y., & Wang, H. (2024). Numerical analysis of the effect of different internal structures on gas-liquid cylindrical cyclone vortices and velocities. International Journal of Chemical Engineering, 2024, 7812685**.**